Journal of Colloid and Interface Science 649 (2023) 492–500

Contents lists available at ScienceDirect

Journal of Colloid And Interface Science

journal homepage: www.elsevier.com/locate/jcis

Interface designing of efficient Z-scheme Ti-$ZnFe_2O_4$/In_2O_3 photoanode toward boosting photoelectrochemical water oxidation

Kaikai Ba, Yinyin Li, Yunan Liu, Yanhong Lin, Dejun Wang, Tengfeng Xie *, Jun Li *

Institute of Physical Chemistry, College of Chemistry, Jilin University, Changchun 130012, PR China

HIGHLIGHT

- The Z-scheme Ti-ZFO/In_2O_3 photoelectrode was successfully constructed.
- Ti-ZFO/In_2O_3 reaches 2.2 mA/cm^2 at 1.23 V vs. RHE, which is 7 times that of pure Ti-ZFO.
- The Z-scheme Ti-ZFO/In_2O_3 could promote the separation and transfer of charges effectively.
- This work provides an effective method and technical means to understanding the Z-scheme mechanism.

GRAPHICAL ABSTRACT

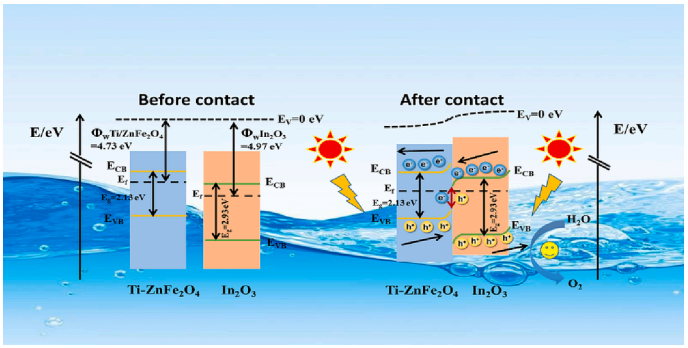

ARTICLE INFO

Keywords:
Ti-$ZnFe_2O_4$/In_2O_3 photoanode
Z-scheme mechanism
Interface electric field
Charge separation
Water oxidation

ABSTRACT

Ti-$ZnFe_2O_4$ photoanode has attracted extensive attention in photoelectrochemical (PEC) water oxidation due to its narrow band gap and good photostability. However, its low efficiency limits its development. Herein, we designed and constructed direct Z-scheme Ti-$ZnFe_2O_4$/In_2O_3 (Ti-ZFO/In_2O_3) photoanode. Under the interface electric field, photogenerated holes with stronger oxidation capacity on In_2O_3 are retained to participate in the water oxidation reaction, and the photocurrent density of Ti-ZFO/In_2O_3 is much higher than that of pure Ti-ZFO, reaching 2.2 mA/cm^2 at 1.23 V vs. RHE. Kelvin Probe, steady-state photovoltage spectroscopy (SPV), transient photovoltage spectroscopy (TPV) and in-situ double beam strategy were used to demonstrate the Z-scheme charge transfer mechanism of Ti-ZFO/In_2O_3 photoanode. Our work provides an effective scheme and technical means for further understanding the mechanism of interfacial charge transfer.

1. Introduction

Using the inexhaustible solar energy splitting water to generate hydrogen is an effective strategy for the preparation of sustainable clean energy [1]. In the water splitting reaction, the oxygen generating half reaction is a four electron process with Gibbs free energy greater than zero, which is more difficult to occur than the two electron process of the hydrogen generating half reaction, and is considered as the speed control step of the entire photoelectrochemical water splitting [2]. Therefore, the search is still on for new photoelectrode materials to improve

* Corresponding authors.
E-mail addresses: xietf@jlu.edu.cn (T. Xie), lj98998@jlu.edu.cn (J. Li).

https://doi.org/10.1016/j.jcis.2023.06.100
Received 11 May 2023; Received in revised form 31 May 2023; Accepted 15 June 2023
Available online 20 June 2023

the overall performance of photocatalysis. In this regard, Zinc ferrite ($ZnFe_2O_4$) could be a promising photoanode material because it has suitable band edge, narrow band gap (2–2.2 eV) especially for excellent photoelectric conversion efficiency, electrochemical stability and low cost [3]. However, the low efficiency of charge separation and transport of $ZnFe_2O_4$ is a key problem to be solved urgently.

Recently, fabrication of Z-scheme heterostructures is also considered as an attractive strategy to overcome the shortcomings of a single semiconductor [4–6]. Generally speaking, when the Z-scheme system is constructed according to the band gap difference between the two semiconductors and the built-in electric field, the electronic ability on the conduction band of semiconductor 1 with weak reduction ability is easy to recombine with the holes on the valence band of semiconductor 2 with weak oxidation ability at the interface, so that the photogenerated hole-electron pairs are effectively separated, and finally the oxidation reaction and reduction reaction are carried out on semiconductor 1 and semiconductor 2, respectively [7]. Based on the above analysis, looking for a semiconductor based Z-scheme photocatalyst system with more correction than $ZnFe_2O_4$ oxidation potential can further improve the water oxidation performance of $ZnFe_2O_4$ photocatalyst.

In recent years, *n*-type semiconductor indium oxide (In_2O_3) with a direct band gap of about 3.7 eV and an indirect band gap of about 2.8 eV has attracted wide attention due to its advantages of stronger oxidation potential, low toxicity and easy film formation [8]. For bare In_2O_3, there are still shortcomings such as narrow visible light absorption range and rapid recombination of hole-electron pairs, which will reduce its visible light catalytic activity. As reported, the formation of heterojunction with semiconductor with good band matching can greatly solve the problems of In_2O_3. In 2021, Li et al. built Fe_2O_3/In_2O_3 Z-scheme catalyst which effective charge separation improved the oxidation production activity of water [9]. In addition, Guo et al. synthesized a new all-solid Z-scheme In_2O_3/Bi_2O_7 heterojunction and used it for the photocatalytic degradation of doxycycline hydrochloride [10]. In 2022, Wan et al. constructed a Z-scheme g-C_3N_4/In_2O_3 heterojunction, which showed excellent performance in photocatalytic CO_2 reduction [11]. Therefore, $ZnFe_2O_4$ with a wide absorption range and a suitable conduction band position (the potential level is about − 1.5 eV) is theoretically suitable for constructing a composite photoanode with In_2O_3 that follows the Z-scheme mechanism, which can further improve the PEC water oxidation performance of $ZnFe_2O_4$.

In this work, we synthesized the Z-scheme mechanism Ti-$ZnFe_2O_4/In_2O_3$ (Ti-ZFO/In_2O_3) composite photoanode by twice hydrothermal. The excellent photoelectrochemical performance of Ti-ZFO/In_2O_3 benefits from strong interface electric field and positive oxidation potential, and the photocurrent density of Ti-ZFO/In_2O_3 was 7 times that of pure Ti-ZFO, reaching 2.2 mA/cm^2 at 1.23 V vs. RHE. We found that the charge transfer between In_2O_3 and Ti-ZFO follows the Z-scheme mechanism, which is demonstrated through Kelvin Probe, steady state photovoltage spectroscopy (SPV), transient photovoltage spectroscopy (TPV) and the in-situ two beam strategy. It shows that under the action of interface electric field, the electrons of In_2O_3 are more inclined to compound with the holes of Ti-ZFO at the interface, which weakens the charge recombination of In_2O_3 itself, and makes more holes of In_2O_3 to participate in the water oxidation reaction. It is believed that our work offers a deeper understanding for Z-scheme mechanism.

2. Experimental section

2.1. Materials

Ferric chloride hexahydrate ($FeCl_3{\cdot}6H_2O$, 97.0%) was purchased from Alfa Aesar Co. LLC. Indium nitrate ($In(NO_3)_3{\cdot}4.5H_2O$, ≥99.0%), Sodium nitrate ($NaNO_3$, ≥99.0%), Titanium tetrachloride ($TiCl_4$, ≥98.0%), Zinc nitrate hexahydrate ($Zn(NO_3)_2{\cdot}6H_2O$, ≥99.0%), Hydrogen peroxide (H_2O_2, 30 wt%) were bought from Sinopharm Chemical Reagent Co., Ltd. Urea (CH_4N_2O, ≥99.0%) was purchased from Beijing Chemical Works Co., Ltd. Potassium hydroxide (KOH, 90%) was obtained from Macklin chemical reagent Co., Ltd. Deionized water with a resistance of 18.2 MΩ was used in the whole experimental process. All materials were used without further purification.

2.2. Sample preparation

2.2.1. Synthesis of Ti-doped $ZnFe_2O_4$

0.81 g ferric chloride hexahydrate, 0.3 g sodium nitrate and 0.62 g zinc nitrate hexahydrate were prepared into 20 ml of uniform transparent solution, and then added 30 μL of 0.05% $TiCl_4$ ethanol solution. The precursor is poured into to a 50 ml autoclave containing cleaned FTO, which reacts for 6 h at 100 °C. The rinsed and dried film was then annealed at 550 °C for 2 h. The final sample was marked as Ti-ZFO.

2.2.2. Synthesis of Ti-ZFO/In_2O_3

In_2O_3 cubes were synthesized on a modified method [12]. 0.12 g indium nitrate pentahydrate and 0.04 g urea were prepared into a 20 ml homogeneous solution, and then the precursor was poured into a 50 ml autoclave containing Ti-ZFO electrode, which reacts at 160 °C. After cooling, the prepared films were rinsed, dried, and is put into muffle furnace for annealing. The resulting composite photoanode is named as Ti-ZFO/In_2O_3. The preparation process of pure In_2O_3 photoanode is the same as the above process, just replace the Ti-ZFO electrode with FTO conductive glass.

2.3. Characterization

The crystal structure of all photoanodes between 20 and 80° was characterized by X-ray diffraction (XRD, Bruker D8 ADVANCE). X-ray photoelectron spectroscopy (XPS, Escalab 250Xi) is used to convey all elements and its status, where the C 1 s peak is at 284.8 eV to calibrate the binding energy. Optical absorption characteristics of all photoanodes were characterized by Ultraviolet–visible (UV–vis) spectra (SHIMADZU UV-3600). Field emission scanning electron microscopy (FE-SEM, Regulus 8100) and transmission electron microscopy (TEM, TALOS F200) were used to characterize the morphology of photoanodes.

The steady-state surface photovoltage (SPV) and transient photovoltage (TPV) spectra were used to characterize the dynamic separation of photogenerated charges. The TPV testing is at 100 μJ 355 nm laser irradiation, including digital oscilloscope (500 MHz, Tektronix), data processor, pulse laser (Polaris II, New Wave Research, Inc.) and signal acquisition amplifier. The SPV testing is carried out between 300 and 800 nm at 24 Hz, including monochromator (ZLolix SBP500), data processor, optical chopper (SR540), phase-locked amplifier (SB830-DPS) and 500 W xenon lamp (CHF-XM-500 W).

2.4. PEC measurements

The electrochemical station (CHI660E) equipped with a standard three electrode system is used for photoelectrochemical measurements under simulated solar illumination (AM 1.5G, 100 mW/cm^2), in which the photoanode, platinum wire and Ag/AgCl are used as the working electrode, the counter electrode and the reference electrode, respectively. The stability measurement of Ti-ZFO/In_2O_3 is carried out at 1.23 V vs. RHE, and the PEIS is carried out in the frequency range of 5×10^{-2}-10^5 Hz under AM 1.5G illumination. The conversion between potentials versus Ag/AgCl and versus RHE was calibrated by Nernst equation ($E_{RHE} = E_{Ag/AgCl} + 0.059pH + E^{\theta}_{Ag/AgCl}$), the electrolyte is 1 M KOH (pH = 13.6), and the reaction area is 0.283 square centimeters.

The bias photon-to-current efficiency can be calculated by the following formula:

$$ABPE = \frac{(J_{light} - J_{dark}) \times (1.23 - V_{RHE})}{P_{light}}$$

where J_{light} and J_{dark} respectively represent the current density of photoanode under light and dark state, V_{RHE} represents the potential under standard hydrogen electrode, $P_{light} = 100$ mW/cm^2.

The conversion efficiency is calculated between the incident photon and the current as follows:

$$IPCE = \frac{J \times 1240}{P_{mono} \times \lambda}$$

where P_{mono} is the irradiation intensity, J is the photocurrent density, λ is the irradiation wavelength, and the wavelength range is 390–590 nm.

The injection efficiency (η_{inj}) and the separation efficiency (η_{sep}) can be calculated from the following formulas:

$$\eta_{inj} = \frac{J_{H_2O}}{J_{H_2O_2}}$$

$$\eta_{sep} = \frac{J_{H_2O_2}}{J_{abs}}$$

where J_{H2O} represents the photocurrent density obtained in 1 M potassium hydroxide, J_{H2O2} represents the photocurrent density obtained in 0.5 M hydrogen peroxide containing potassium hydroxide, and J_{abs} represents that all photons absorbed by the photoanode are converted into photocurrent.

The carrier concentration (N_d) is calculated by the following formula:

$$\frac{1}{C^2} = \frac{2}{e\epsilon\epsilon_{0Nd}}\left[(V - V_{fb}) - \frac{kT}{e}\right]$$

where e, ε_0, ε are 1.60 × 10^{-19}, 8.85 × 10^{-14}F cm^{-1}, 80 ($ZnFe_2O_4$), respectively.

3. Results and discussions

3.1. Synthesis and characterization

Firstly, $ZnFe_2O_4$ nanorods were synthesized on FTO by hydrothermal method and Ti^{4+} was used to improve their conductivity (Scheme 1). Then, an InOOH layer was grown on Ti-$ZnFe_2O_4$ by in situ hydrothermal reaction for 6 h, and converted to In_2O_3 after annealing in air. The final photoanode is named as Ti-ZFO/In_2O_3.

From the SEM images in Fig. 1(a) and Fig. S1(a), the pure Ti-ZFO is composed of nanorod arrays with a diameter of about 60 nm closely arranged, while the pure In_2O_3 is cubic block structure [13]. When In_2O_3 was loaded on Ti-ZFO nanorods, as shown in Fig. 1(b), the cubes completely covered the nanorod array. From Fig. 1(c) and Fig. 1(d), we can clearly see that a layer of In_2O_3 cubes is uniformly loaded on the top of the nanorods, and the nanorods are uniformly loaded with a layer of In_2O_3 cubes. The surface of Ti-ZFO/In_2O_3 is also loaded with a layer of In_2O_3 small particles, which fully proves the successful construction of Ti-ZFO/In_2O_3. The microstructure and morphology were further observed from the Ti-ZFO/In_2O_3 TEM images in Fig. 1(e) and Fig. S1(b), in which the 0.252 nm and 0.282 nm lattice stripes correspond to the $ZnFe_2O_4$ (311) plane and In_2O_3 (222) plane, respectively [14,15]. Through EDS element mapping analysis in Fig. 1(f), Fe, O, Zn, In and Ti is clearly revealed, which further proves that the successful preparation of Ti-ZFO/In_2O_3.

From the XRD pattern of Ti-ZFO, In_2O_3 and Ti-ZFO/In_2O_3 in Fig. 2 (a), the characteristic diffraction peaks of Ti-ZFO and Ti-ZFO/In_2O_3 at 35.6° correspond to the (311) crystal plane of ZFO, and are consistent with the standard card of ZFO (PDF#73-1963) [16]. Meanwhile, Ti-ZFO/In_2O_3 has a very obvious characteristic diffraction peak at 30.6° in Fig. 2(b), which is consistent with the In_2O_3 standard card (PDF#06-0416), proving that In_2O_3 was successfully prepared and loaded on Ti-ZFO [17].

Fig. 2(c) is the XPS full spectrum of the composite photoanode, which confirms the coexistence of Fe, In, Zn and O in the sample. The O 1 s orbital can be simulated to two peaks at 530.58 and 529.08 eV, corresponding to hydroxyl oxygen (OH^-) and lattice oxygen (Fig. 2(d)), respectively [18,19]. In addition, Fig. S2(a) is the Zn 2p orbital XPS spectrum at 1021 eV [5]. The two characteristic peaks of Ti 2p appeared at 463.5 eV and 457.8 eV in Fig. S2 (b), proving that Ti^{4+} was successfully doped into the ZFO photoanode [20].

3.2. PEC properties of Ti-$ZnFe_2O_4$/In_2O_3 photoanodes

The PEC performances of Ti-ZFO, Ti-ZFO/In_2O_3 and In_2O_3 were tested by J-V curves in 1 M KOH [21]. Compared with Ti-ZFO and In_2O_3, the photoelectrochemical performance of Ti-ZFO/In_2O_3 has been significantly improved (Fig. 3(a)), and its photocurrent density reached 2.2 mA/cm^2 at 1.23 V vs. RHE, 7 times that of Ti-ZFO. In addition, the performance of Ti-ZFO/xh-In_2O_3 reaches the optimal value when the reaction time is 6 h (Fig. S3). From Fig. 3(b), Ti-ZFO/In_2O_3, Ti-ZFO and In_2O_3 photoanodes all showed good photoresponse in the range of 390–590 nm, and the IPCE value of Ti-ZFO/In_2O_3 was 29.5% at 390 nm, much higher than that for Ti-ZFO alone (10.2%) and In_2O_3 (9.3%). Moreover, Ti-ZFO/In_2O_3 achieved the highest ABPE value of 0.19 % in Fig. 3(c) and it can maintain photostability for PEC water oxidation reaction in Fig. 3(d).

A series of photoelectrochemical tests show that the construction of Ti-ZFO/In_2O_3 composite photoanode improves the In_2O_3 photocatalytic water oxidation performance. Generally speaking, the improvement of PEC performance is determined by the optical absorption, separation efficiency and injection efficiency of the photoanode [22,23]. Compared with Ti-ZFO, the band gap of Ti-ZFO/In_2O_3 composite photoanode did not change significantly in Fig. S4, while pure In_2O_3 begins to absorb near 425 nm, which means that In_2O_3 contributes less to the light absorption of Ti-ZFO/In_2O_3, and the light absorption is not the dominant factor.

3.3. Separation and transport of photogenerated charges

To explore the separation and transmission of composite photoanode photogenerated charges, we calculated the open-circuit photovoltage

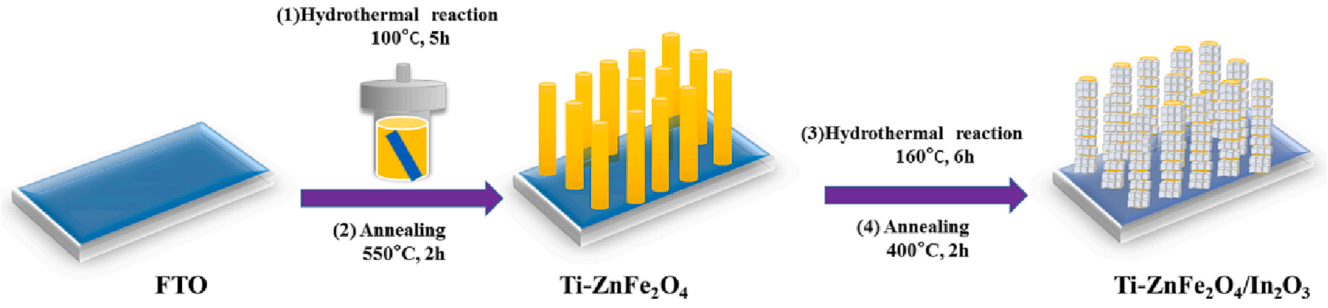

Scheme 1. Schematic of the synthesis process of Ti-ZFO/In_2O_3 photoanode.

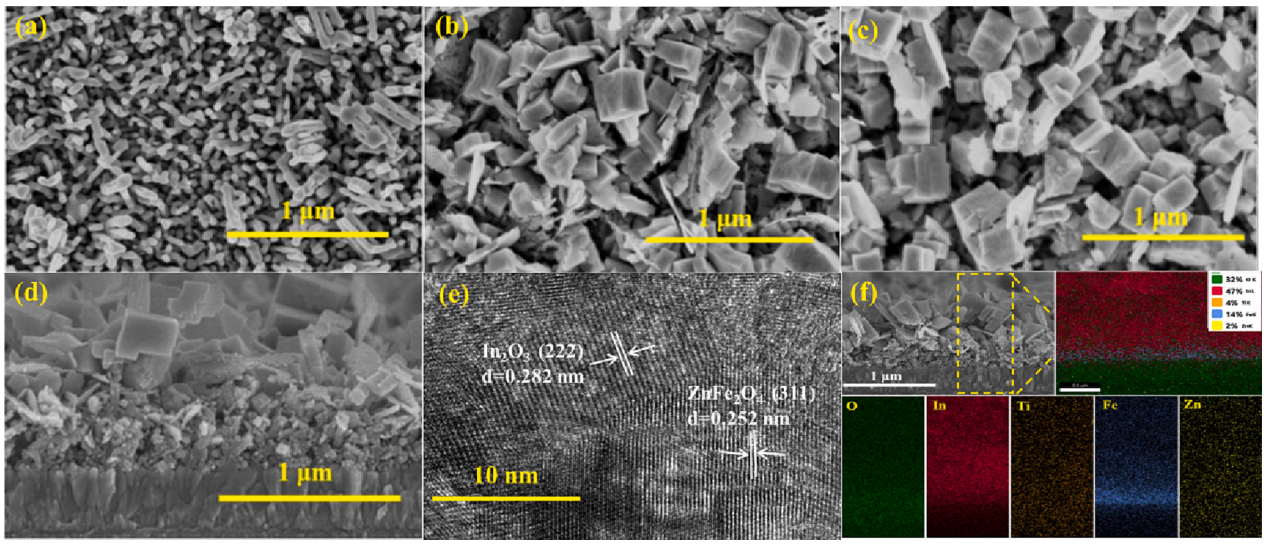

Fig. 1. SEM images of (a) Ti-ZFO, (b) In_2O_3, (c) Ti-ZFO/In_2O_3. (d) The section image of Ti-ZFO/In_2O_3 film. (e) HR-TEM image of Ti-ZFO/In_2O_3. (f) elemental mapping of Fe, Ti, In, O, Zn of Ti-ZFO/In_2O_3.

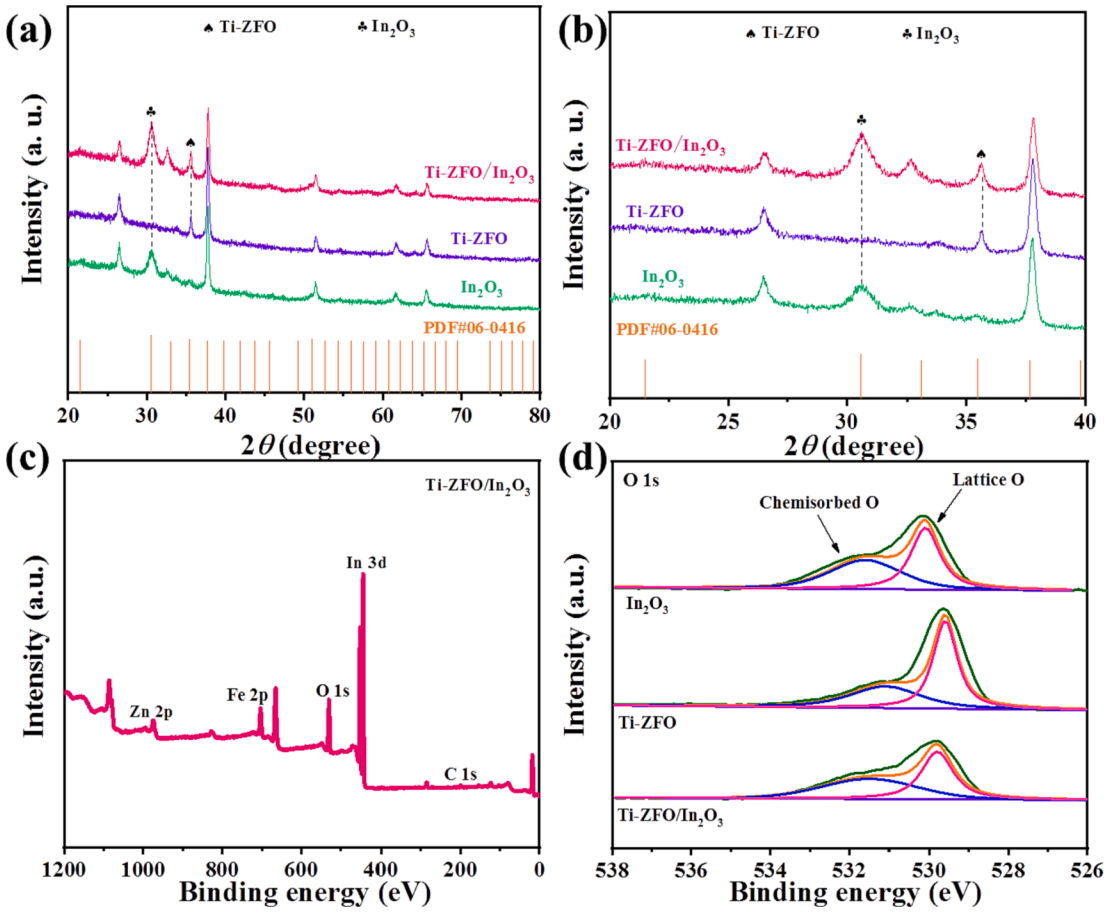

Fig. 2. XRD patterns of (a) Ti-ZFO/In_2O_3, Ti-ZFO and In_2O_3. (b) enlarged XRD patterns in the range of 20-40°. XPS spectra of Ti-ZFO/In_2O_3, Ti-ZFO and In_2O_3 photoanodes (c) XPS survey spectra of Ti-ZFO/In_2O_3, XPS spectra of photoanodes (d) O1s.

(OCPV) in 1 M KOH [24]. The ΔOCPV value ($OCPV_{dark} - OCPV_{light}$) of the Ti-ZFO/$In_2O_3$ is higher than those of pure Ti-ZFO and In_2O_3 in Fig. 4 (a), indicating that the enhancement of surface self built electric field further promotes the charge separation in Ti-ZFO/In_2O_3 heterojunction. The linear sweep voltammetry curves (LSV) obtained in an electrolyte containing a hole scavenger (H_2O_2) are shown in Fig. S5. The introduction of In_2O_3 significantly improves the η_{inj} and η_{sep} values of Ti-ZFO photoanode from 9% to 52% and 3% to 20% at 1.23 V vs. RHE (Fig. 4(b) and (c)), respectively. The increased η_{inj} indicates that Ti-ZFO/In_2O_3 composite photoanode possesses faster water oxidation kinetics. Fig. 4(d) shows that Ti-ZFO/In_2O_3 composite photoanode has the smallest sharp peak, which indicates that the interface transport of

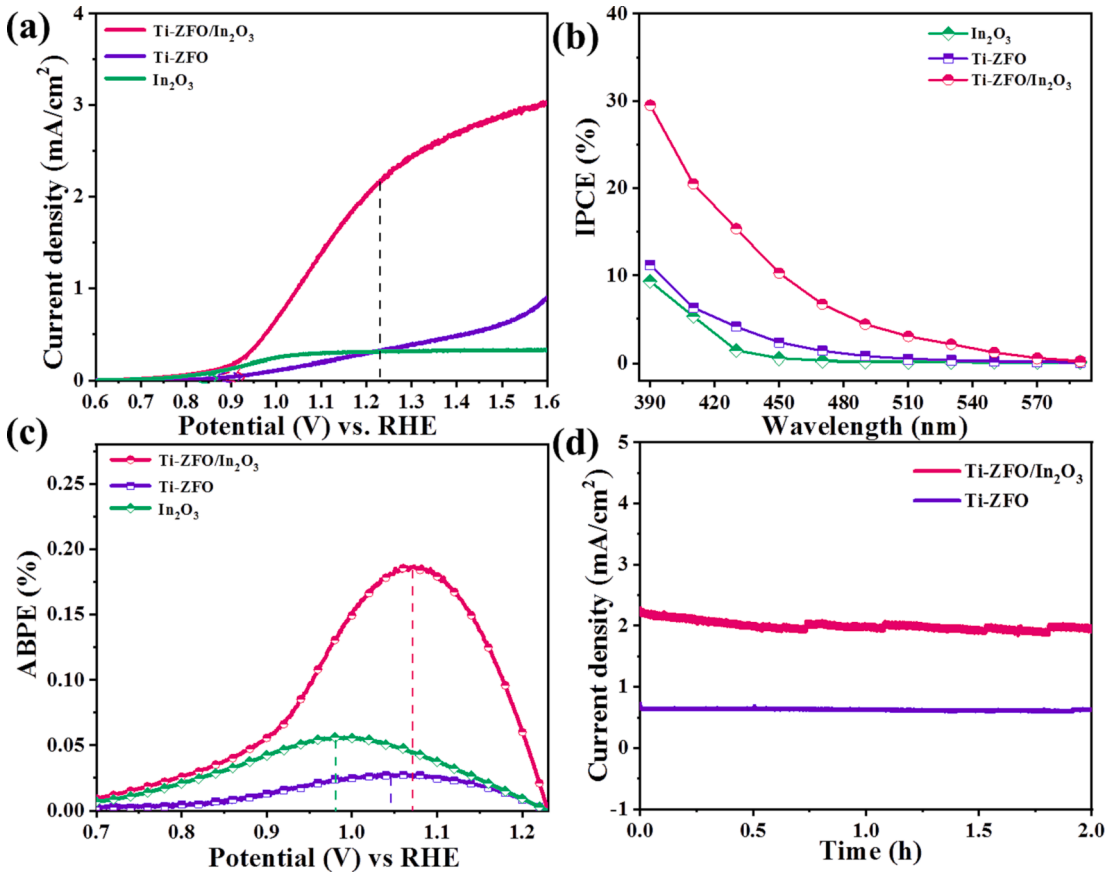

Fig. 3. (a) J-V curves under AM 1.5G irradiation, (b) IPCE values from 390 to 590 nm, (c) ABPE values of Ti-ZFO/In_2O_3, Ti-ZFO and In_2O_3. (d) Photostability measurement of Ti-ZFO/In_2O_3 and Ti-ZFO.

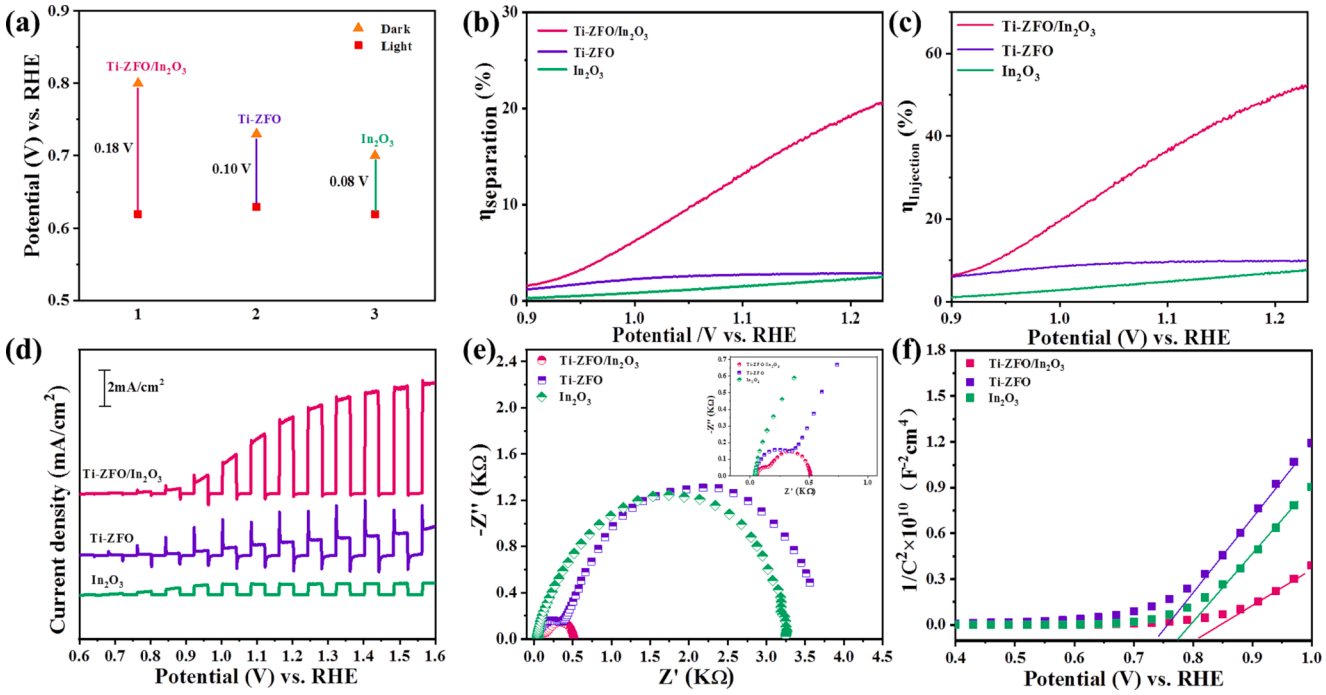

Fig. 4. (a) Opencircuit potentials (OCPV) in 1 M KOH electrolyte, (b) Separation efficiency, (c) Injection efficiency, (d) LSV curves under modulated light, (e) EIS at 1.0 V vs. RHE, (f) Mott-Schottky plots in dark of Ti-ZFO/In_2O_3, Ti-ZFO and In_2O_3 photoanodes.

charges is more smooth after the introduction of In_2O_3, and the photogenerated holes are injected into the solution more rapidly [25].

The transport capacity of photogenerated charges at the interface is further measured by electrochemical impedance spectroscopy (EIS) [26]. As shown in Fig. 4(e), Ti-ZFO/In_2O_3 showed the smallest radius in both low-frequency and high-frequency regions compared with pure Ti-ZFO and In_2O_3, indicating the most smooth charge charge transmission at the solid–solid interface and the solid–liquid interface [27]. Besides, we also fit the Nyquist point by the equivalent circuit diagram, as shown in Fig. S6, R_{bulk} (115.4 Ω) and R_{ct} (346.1 Ω) of Ti-ZFO/In_2O_3 are smaller than those of pure Ti-ZFO and In_2O_3 in Table 1, indicating that the construction of Ti-ZFO/In_2O_3 photoanode can effectively enhance charge transmission capability [28]. The slopes of Mott Schottky curves are shown as positive values for all photoanodes in Fig. 4(f), which indicates that the Ti-ZFO, In_2O_3 and Ti-ZFO/In_2O_3 photoanodes all exhibit the properties of *n*-type semiconductors, that is, electrons are the majority current-carrying properties [29]. After calculation, the carrier concentrations of Ti-ZFO, In_2O_3, and Ti-ZFO/In_2O_3 are 4.06×10^{19}, 4.95×10^{19} and 1.56×10^{20} cm^{-3}, respectively. The excellent conductivity indicates the rapid charge separation and transport in Ti-ZFO/In_2O_3 [30].

3.4. Z-scheme charge transfer mechanism

To further explore the reasons for charge separation and injection enhancement, we investigated the charge transfer mechanism between Ti-ZFO and In_2O_3. As we all know, the interface electric field determines the charge separation between the two semiconductors, which is further determined by the Fermi energy difference [31,32]. On this basis, we tested the WF (Φ) of the sample using the Kelvin probe to study the Ti-ZFO/In_2O_3 interface driving force [33]. The WF values of Ti-ZFO and In_2O_3 were obtained from the following equation:

$$\Phi_{sample} = \Phi_{Au} + eCPD\,(\Phi_{Au} = 4.8eV).$$

The CPD values of Ti-ZFO and In_2O_3 are −152 and 80 mV (Fig. 5), respectively. And the WF values of Ti-ZFO and In_2O_3 are 4.73 eV and 4.97 eV after calculation, respectively. The above results indicate that the Fermi level of Ti-ZFO is higher than that of In_2O_3, that is, Ti-ZFO can form an upward bend, while In_2O_3 can form a downward bend upon contact, which facilitates the transfer of electrons from In_2O_3 to Ti-ZFO. Obviously, we can reasonably assume that the holes of Ti-ZFO combine with electrons of In_2O_3, resulting in the transfer of holes of In_2O_3 to the surface for water oxidation. Based on the interfacial driving force analysis, we know that the interfacial charges migration process of Ti-ZFO/In_2O_3 could follow the Z-scheme mechanism.

After the successful construction of Ti-ZFO/In_2O_3 composite photoanode, the existence of interface electric field has a positive impact on charge transfer and transport. Thus, the steady-state surface photovoltage spectrum (SPV) and the transient surface photovoltage spectrum (TPV) were conducted to investigate the transfer behavior of the charge, as we all know, the positive response represents the holes transfer to the sample surface, the negative response indicates the electrons transfer to the surface, and the stronger response represents higher charge separation efficiency [5]. For the SPV spectrum (In_2O_3 side illumination) of the Ti-ZFO/In_2O_3 photoanode at 300–800 nm in Fig. 6(a), we can see that the positive signal of Ti-ZFO/In_2O_3 composite photoanode is significantly stronger than that of pure In_2O_3, indicating that under the interface electric field, the holes of Ti-ZFO valence band and the

Table 1
EIS fitting results of Ti-ZFO/In_2O_3, Ti-ZFO and In_2O_3 photoanodes.

Photoanode	Rs(Ω)	Rbulk (Ω)	CPE1(F.cm^{-2})	R_{ct} (Ω)	CPE2(F.cm^{-2})
In_2O_3	42.64	314.7	6.165×10^{-6}	3506	1.532×10^{-4}
Ti-ZFO	41.18	146.7	1.755×10^{-5}	3100	1.842×10^{-5}
Ti-ZFO/In_2O_3	52.81	115.4	2.544×10^{-5}	346.1	1.945×10^{-4}

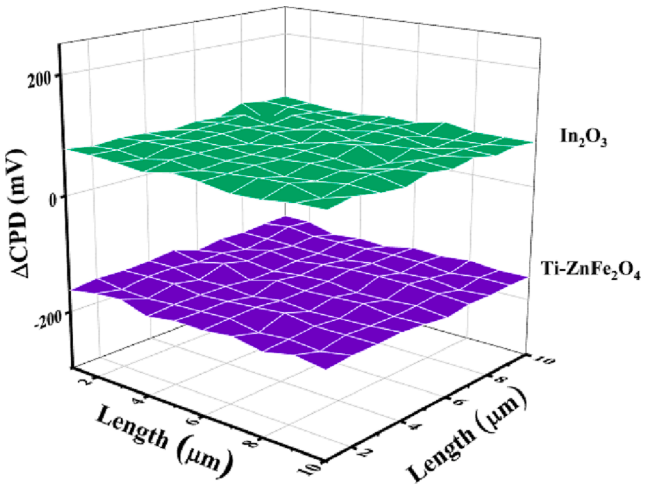

Fig. 5. Work Function measurements of pure Ti-ZFO and In_2O_3.

electrons of In_2O_3 conduction band recombine at the interface, which enables more holes of In_2O_3 to migrate to the surface [34]. To investigate the kinetic behavior of photogenerated charges, transient surface photovoltage (TPV) measurements were performed under 355 nm laser irradiation. From Fig. 6(b), the TPV response of Ti-ZFO/In_2O_3 is higher than that of pure In_2O_3, which further proves the rapid charge separation of Ti-ZFO/In_2O_3. Therefore, the interface electric field constructed by Ti-ZFO and In_2O_3 in the composite photoanode is conducive to the separation and transmission of charge, clarifying the Z-scheme mechanism of Ti-ZFO/ In_2O_3 [35].

Subsequently, we changed the illumination mode to deeply explore the transfer behavior of charges at the interface [36]. Briefly, the Ti-ZFO side is illuminated with 300–800 nm monochromatic light, and the measured result is the photovoltage signal on the Ti-ZFO side. The SPV spectrum of the Ti-ZFO/In_2O_3 photoanode shows a more negative signal than that of pure In_2O_3 (Fig. 6(c)), indicating that when the Ti-ZFO side is illuminated, the photogenerated hole-electron pairs are rapidly separated under the interface electric field, and the holes of the Ti-ZFO are easier to recombine with the electrons of In_2O_3 at the interface, so that more electrons on Ti-ZFO migrate to the illumination side to show a more negative signal. Fig. 6(d) shows the TPV spectrum (Ti-ZFO side illumination) of Ti-ZFO/In_2O_3 photoanode excited under 355 nm pulsed laser irradiation. The Schottky barrier between FTO and Ti-ZFO causes the photogenerated holes to migrate to the FTO side, thus showing a positive signal in a short time [37]. After the introduction of In_2O_3, the holes generated by Ti-ZFO are easy to combine with the electrons of In_2O_3 under the interface electric field. In a long time, the negative signal of TPV mainly detects the behavior of electrons migrating to the Ti-ZFO surface. Due to the combination of the holes of Ti-ZFO and the electrons of In_2O_3, more electrons on Ti-ZFO migrate to the illumination side, showing a more negative signal, such as SPV spectrums, thus proving the Z-scheme charge transfer mechanism of Ti-ZFO/In_2O_3.

The Z-scheme mechanism is a two-photon process, and in order to make Ti-ZFO and In_2O_3 fully photoexcited, we adopted a two beam strategy based on TPV spectrum to deeply explore the transfer behavior of the interface charge of Ti-ZFO/In_2O_3 photoanode [16]. When the sample is irradiated by 355 nm and 365 nm pulsed laser from In_2O_3 side and Ti-ZFO side respectively, the interface electric field is further enhanced under the double beam, so that the TPV response of Ti-ZFO/In_2O_3 is higher in Fig. 7(a). The electrons of In_2O_3 are more easily recombined with the holes of Ti-ZFO, which more holes on In_2O_3 that are not recombined with electrons migrate to the surface, and the positive signal is further enhanced. When the illumination direction was changed to monitor the behavior of photogenerated electrons migrating to the Ti-ZFO surface in Fig. 7(b), it is found that the positive signal at

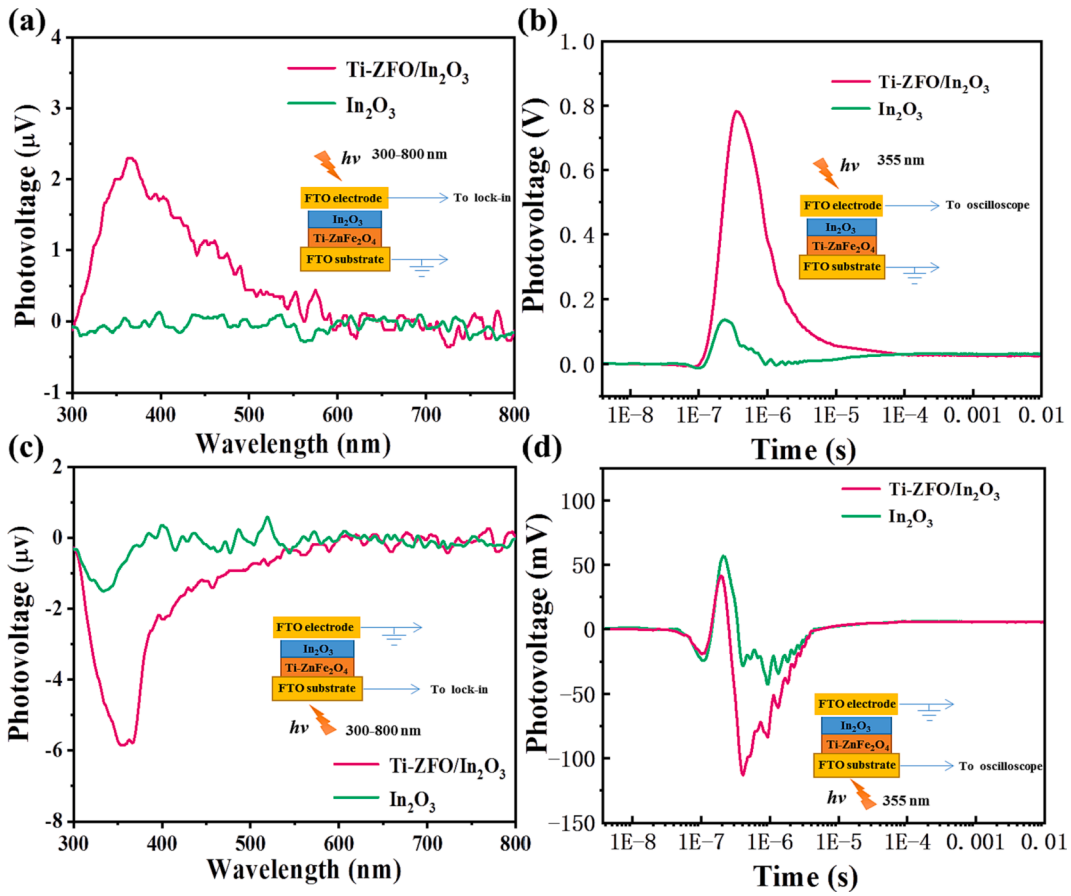

Fig. 6. (a) SPV response when illuminating from In_2O_3 side. (b) TPV response when illuminating from In_2O_3 side under 100 μJ laser irradiation. (Laser wavelength: 355 nm). (c) SPV response when illuminating from Ti-ZFO side. (d) TPV response when illuminating from Ti-ZFO side. The insets show the illumination mode of SPV and TPV measurements.

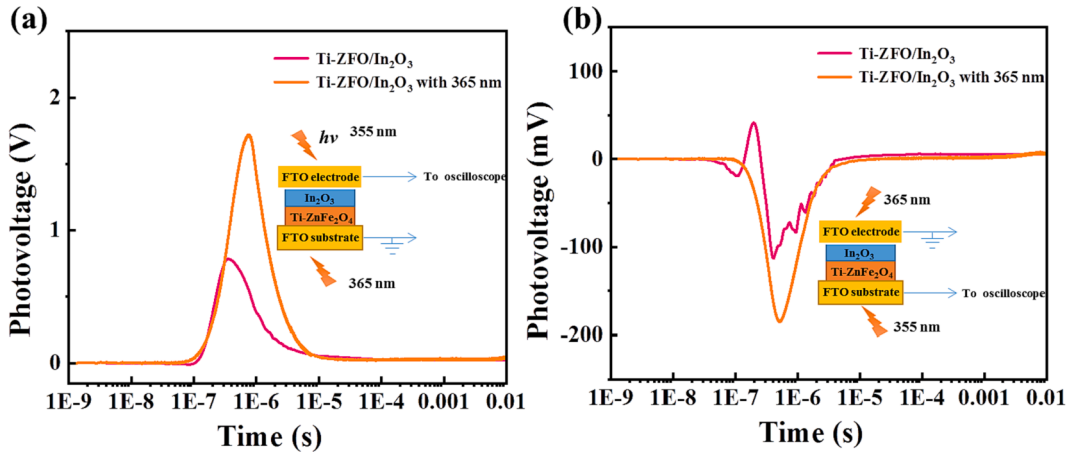

Fig. 7. TPV response of (a) Ti-ZFO side (Laser:365 nm) and In_2O_3 side (Laser:355 nm). (b) Ti-ZFO side (Laser:355 nm) and In_2O_3 side (Laser:365 nm). The insets show the illumination mode of TPV measurement.

1.9×10^{-7} s obviously weakened, indicating that the Schottky barrier between Ti-ZFO and FTO is reduced, and more electrons can migrate to Ti-ZFO side, thus showing stronger negative response.

In order to fully explore the two-photon process, we carried out in-situ double beam measurement based on the PEC three electrode system for the two-dimensional ordered Ti-ZFO/In_2O_3 photoanode. As shown in Fig. S7, we adopt 365 nm laster is uesd to excite In_2O_3, while the Ti-ZFO side is illuminated by xenon lamp (AM 1.5G). From Fig. 8(a), we only use single beam to illuminate Ti-ZFO/In_2O_3, the photocurrent is 2.0 and 1.8 mA/cm^2 at 1.23 V vs. RHE, respectively. When Ti-ZFO/In_2O_3 is illuminated with double beams, the photocurrent density can reach 4.6 mA/cm^2 at 1.23 V vs. RHE, which verifies the two-photon process of Ti-ZFO/In_2O_3. The excellent PEC performance can be attributed to the enhanced interface electric field under double beams illumination, leading to more holes of In_2O_3 to oxidize water, which is consistent with Z-scheme mechanism previously analyzed. The

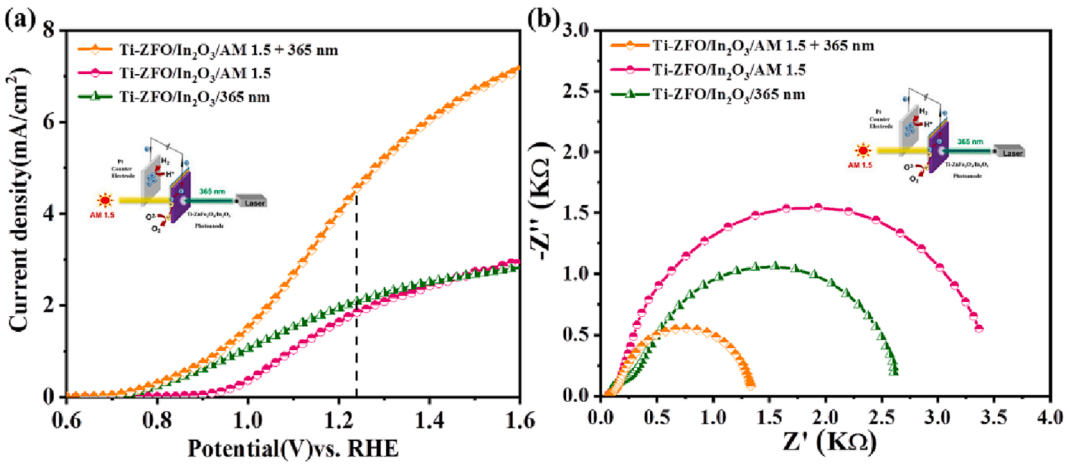

Fig. 8. (a) J-V curves of Ti-ZFO/In_2O_3 under double beams (AM 1.5G + 365 nm) and single beam (AM 1.5G or 365 nm). (b) EIS of Ti-ZFO/In_2O_3 at 1.0 V vs. RHE under double beams and single beam (AM 1.5G).

electrochemical impedance spectroscopy under double beams has made a detailed exploration of the transmission resistance of charges at the interface in Fig. 8(b). Compared with single beam irradiation, the radius of semicircle in both high frequency and low frequency regions under the simultaneous irradiation of double beams is significantly reduced, which means that the enhanced interface electric field promotes the separation and transmission of charges at the interface [38]. The above experimental results indicate that the charge transfer between In_2O_3 and Ti-ZFO follows the Z-scheme mechanism.

In addition, XPS spectra can also be used to further determine the direction of electron migration in the Ti-ZFO/In_2O_3 system. As shown in Fig. 9(a), after the formation of Ti-ZFO/In_2O_3, the In 3d peak positively shifted compared with pure In_2O_3, which indicates that the electron density of In_2O_3 side in Ti-ZFO/In_2O_3 decreases, indirectly indicating that more electrons are consumed at the interface [9]. Furthermore, compared with pure Ti-ZFO, the Fe 2p peak of Ti-ZFO/In_2O_3 composite photoanode has a negative shift in Fig. 9(b), which indicates that the electron density increases in Ti-ZFO side and more holes are compounded at the interface.

The Ti-ZFO/In_2O_3 photoanode after stability test was analyzed by XPS, XRD and SEM. As shown in the Fig. S8(a) and S8(c), the In_2O_3 cube on the Ti-ZFO nanorod became slightly rough, but the overall morphology did not change much, and the morphology of the In_2O_3 photoanode also changed little after the stability test (Fig. S8(b) and S8 (d)). After the stability test, the characteristic diffraction peak of In_2O_3 can still be found at 30.6° in the XRD pattern of Ti-ZFO/In_2O_3 (Fig. S9 (a)), indicating that the synthesized In_2O_3 has good stability in alkaline environment. From the XPS results of Ti-ZFO/In_2O_3, it can be seen that the surface chemical environment of In has hardly changed after the reaction in the Fig. S9(b)-S9(d).

Based on the above analysis, the schematic diagram of charge transfer in Ti-ZFO/In_2O_3 is shown in Scheme 2. When Ti-ZFO and In_2O_3 are in contact, in the process of Fermi level leveling, Ti-ZFO forms an upward band bend while In_2O_3 forms a downward band bend, and the composite photoanode thus forms the interface electric field directed from Ti-ZFO to In_2O_3. Under the interface electric field, the In_2O_3 electrons on low conduction band will combine with the Ti-ZFO holes with high valence band, and more In_2O_3 holes on strong oxidation ability will participate in the water oxidation reaction.

4. Conclusions

In summary, the Z-scheme Ti-$ZnFe_2O_4$/In_2O_3 (Ti-ZFO/In_2O_3) composite photoanode was successfully constructed, and its photocurrent density reached 2.2 mA/cm^2 at 1.23 V vs. RHE, 7 times that of Ti-ZFO. We investigated the charge transfer behavior between In_2O_3 and Ti-ZFO in detail through Kelvin Probe, surface photovoltage technique and in-situ two beam strategy, which shows that the electrons of In_2O_3 are more inclined to compound with the holes of Ti-ZFO at the interface, while more holes migrating to the surface of In_2O_3 to participate in the water oxidation reaction, thus greatly improving the photocatalytic performance of Ti-ZFO. It is believed that our work provides an effective

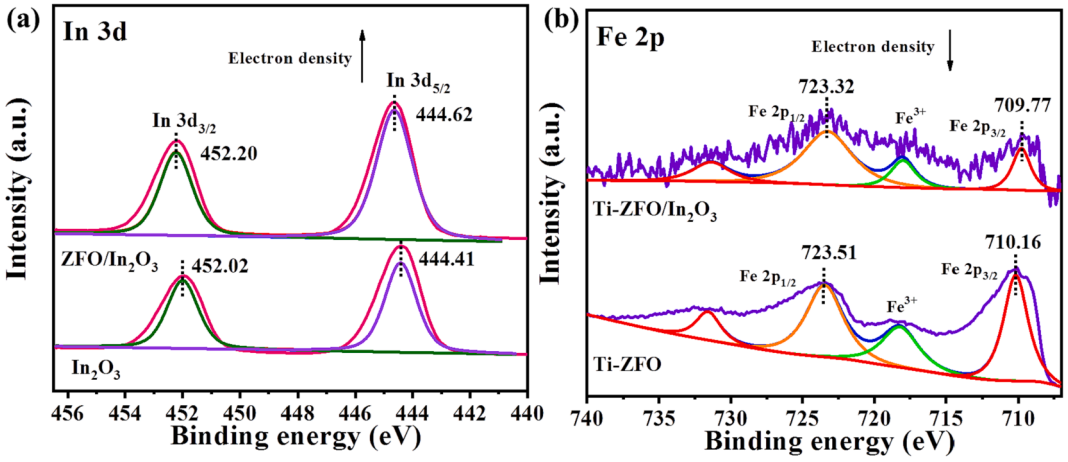

Fig. 9. XPS (a) In 3d for Ti-ZFO/In_2O_3 and In_2O_3. (b) Fe 2p for Ti-ZFO/In_2O_3 and Ti-ZFO.

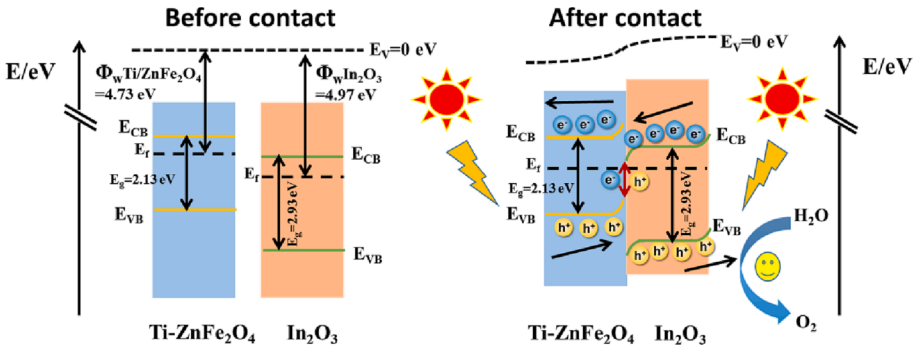

Scheme 2. Band changes of Ti-ZFO and In_2O_3 before and after contact.

and novel means to prove the Z-scheme charge transfer in PEC water oxidation.

CRediT authorship contribution statement

Kaikai Ba: Conceptualization, Investigation, Validation, Writing – original draft. **Yinyin Li:** Methodology, Investigation. **Yunan Liu:** Investigation. **Yanhong Lin:** Writing – review & editing. **Dejun Wang:** Writing – review & editing. **Tengfeng Xie:** Project administration, Conceptualization, Supervision. **Jun Li:** Conceptualization, Supervision.

Declaration of Competing Interest

The authors declare that they have no known competing financial interests or personal relationships that could have appeared to influence the work reported in this paper.

Data availability

Data will be made available on request.

Acknowledgements

This work was financially supported by the National Natural Science Foundation of China (Grant Nos. 22172057, 21773086, 21872063).

Appendix A. Supplementary material

Supplementary data to this article can be found online at https://doi.org/10.1016/j.jcis.2023.06.100.

References

[1] H. Wu, L. Zhang, A. Du, R. Irani, R. van de Krol, F.F. Abdi, Y.H. Ng, Nat. Commun. 13 (2022) 6231.
[2] C.S. Ahart, K.M. Rosso, J. Blumberger, J. Am. Chem. Soc. 144 (2022) 4623–4632.
[3] S. Kim, M.A. Mahadik, A. Periyasamy, W.-S. Chae, J. Ryu, S.H. Choi, J.S. Jang, Catal. Sci. Technol. 11 (2021) 3141–3152.
[4] S. Li, P. Ge, T. Hang, H. Zhou, F. Guo, Y. Wu, C. Li, Appl. Surf. Sci. 610 (2023), 155454.
[5] H. Sun, C. Dong, Q. Liu, Y. Yuan, T. Zhang, J. Zhang, Y. Hou, D. Zhang, X. Feng, Adv. Mater. 32 (2020) 2002486.
[6] F. Xing, C. Cheng, J. Zhang, Q. Liu, C. Chen, C. Huang, Appl. Catal. B 285 (2021), 119818.
[7] Y. Liu, M. Xia, L. Yao, M. Mensi, D. Ren, M. Gratzel, K. Sivula, N. Guijarro, Adv. Funct. Mater. 31 (2021) 2010081.
[8] L. Chen, W. Zhang, Appl. Surf. Sci. 301 (2014) 428–435.
[9] Y. Li, Q. Wu, Y. Chen, R. Zhang, C. Li, K. Zhang, M. Li, Y. Lin, D. Wang, X. Zou, T. Xie, Appl. Catal. B Environ. 290 (2021), 120058.
[10] Z. Pan, L. Qian, J. Shen, J. Huang, Y. Guo, Z. Zhang, Chem. Eng. J. 426 (2021), 130385.
[11] R. Chen, H. Yin, L. Wang, Z. Zhang, J. Ding, J. Zhang, H. Wan, G. Guan, J. Colloid Interface Sci. 631 (2023) 122–132.
[12] J.B. Mu, B. Chen, M.Y. Zhang, Z.C. Guo, P. Zhang, Z.Y. Zhang, Y.Y. Sun, C.L. Shao, Y.H. Liu, ACS Appl. Mater. Interfaces 4 (2012) 424–430.
[13] S.R. Kim, M.A. Mahadik, W.S. Chae, J.H. Ryu, S.H. Choi, J.S. Jang, Appl. Surf. Sci. 513 (2020), 145528.
[14] Y. Xing, W. Que, X. Yin, Z. He, X. Liu, Y. Yang, J. Shao, L. Kong, Appl. Surf. Sci. 387 (2016) 36–44.
[15] Y. Lan, Z. Liu, Z. Guo, M. Ruan, Y. Xin, J. Colloid Interface Sci. 552 (2019) 111–121.
[16] C. Li, S. Li, C. Xu, K. Ma, Nanoscale 13 (2021) 4654–4659.
[17] Y. Yin, X. Wang, L. Li, J. Hei, Y. Han, L. Li, M. Li, Chemelectrochem 7 (2020) 4398–4404.
[18] M.A. Gaikwad, U.P. Suryawanshi, U.V. Ghorpade, J.S. Jang, Small 18 (2022) 2105084.
[19] Q. Bu, X. Liu, Q. Zhao, G. Lu, X. Zhu, Q. Liu, T. Xie, J. Colloid Interface Sci. 626 (2022) 345–354.
[20] Q. Bu, S. Li, Q. Wu, Y. Lin, D. Wang, X. Zou, T. Xie, Catal. Sci. Technol. 9 (2019) 5812–5818.
[21] F. Liu, R. Shi, Z. Wang, Y. Weng, C.M. Che, Y. Chen, Angew. Chem., Int. Ed. 58 (2019) 11791–11795.
[22] H. Zhou, X.D. Zhu, P. Ge, T. Hang, S. Li, F. Guo, Y. Wu, C. Li, Appl. Surf. Sci. 605 (2022), 154693.
[23] K. Ba, Y. Li, R. Zhang, K. Zhang, Z. Liang, Y. Liu, Y. Lin, D. Wang, T. Xie, Int. J. Hydrogen Energy 48 (2023) 3511–3519.
[24] Q. Bu, S. Li, K. Zhang, Y. Lin, D. Wang, X. Zou, T. Xie, ACS Sustain. Chem. Eng. 7 (2019) 10971–10978.
[25] X. Yang, Z. Chen, X. Yue, X. Du, X. Hou, L. Zhang, D. Chen, S. Yi, Small (2022) 2205246.
[26] R. Shen, C. Jiang, Q. Xiang, J. Xie, X. Li, Appl. Surf. Sci. 471 (2019) 43–87.
[27] N. Duc Quang, P. Cao Van, S. Majumder, J.-R. Jeong, D. Kim, C. Kim, J. Colloid Interf. Sci. 616 (2022) 749–758.
[28] Y. Li, Q. Wu, Q. Bu, K. Zhang, Y. Lin, D. Wang, X. Zou, T. Xie, Chin. J. Catal. 42 (2021) 762–771.
[29] X. Liu, C. Bie, B. He, B. Zhu, L. Zhang, B. Cheng, Appl. Surf. Sci. 554 (2021) 149622–149629.
[30] L. Li, R. Zhang, Y. Lin, D. Wang, T. Xie, Chem. Eng. J. 453 (2023), 139970.
[31] H. Li, H. Liu, F. Wang, G. Li, X. Wang, Z. Tang, Nano Res. 15 (2022) 5824–5830.
[32] Q. Bu, S. Li, Q. Wu, L. Bi, Y. Lin, D. Wang, X. Zou, T. Xie, ChemSusChem 11 (2018) 3486–3494.
[33] Y. Li, Y. Chen, Q. Wu, R. Zhang, M. Li, Y. Lin, D. Wang, T. Xie, Catal. Sci. Technol. 12 (2022) 250–258.
[34] Y. Zhang, W. Guo, Y. Zhang, W.D. Wei, Adv. Mater. 33 (2021) 2006654.
[35] J. Abdul Nasir, A. Munir, N. Ahmad, et al., Adv. Mater. 33 (2021) 2105195.
[36] J. Han, Y. Lan, Q. Song, H. Yan, J. Kang, Y. Guo, Z. Liu, Chem. Commun. 56 (2020) 13205–13208.
[37] R. Zhang, H. Wang, Y. Li, D. Wang, Y. Lin, Z. Li, T. Xie, ACS Sustainable Chem. Eng. 9 (2021) 7286–7297.
[38] L. Cao, K. Xu, M. Fan, J. Power Sources 482 (2021), 228956.